2024 IEEE International Conference on Robotics and Automation (ICRA 2024)
May 13-17, 2024. Yokohama, Japan

MPS: A New Method for Selecting the Stable Closed-Loop Equilibrium Attitude-Error Quaternion of a UAV During Flight

Francisco M. F. R. Gonçalves, Ryan M. Bena, Konstantin I. Matveev, and Néstor O. Pérez-Arancibia

***Abstract*— We present *model predictive selection* (MPS), a new method for selecting the stable *closed-loop* (CL) equilibrium *attitude-error quaternion* (AEQ) of an *uncrewed aerial vehicle* (UAV) during the execution of high-speed yaw maneuvers. In this approach, we minimize the cost of yawing measured with a *performance figure of merit* (PFM) that takes into account both the aerodynamic-torque control input and attitude-error state of the UAV. Specifically, this method uses a control law with a term whose sign is dynamically switched in real time to select, between two options, the torque associated with the lesser cost of rotation as predicted by a dynamical model of the UAV derived from first principles. This problem is relevant because the selection of the stable CL equilibrium AEQ significantly impacts the performance of a UAV during high-speed rotational flight, from both the power and control-error perspectives. To test and demonstrate the functionality and performance of the proposed method, we present data collected during one hundred real-time high-speed yaw-tracking flight experiments. These results highlight the superior capabilities of the proposed MPS-based scheme when compared to a benchmark controller commonly used in aerial robotics, as the PFM used to quantify the cost of flight is reduced by $60.30\,\%$, on average. To our best knowledge, these are the first flight-test results that thoroughly demonstrate, evaluate, and compare the performance of a real-time controller capable of selecting the stable CL equilibrium AEQ during operation.**

I. Introduction

A significant number of schemes developed for controlling the attitude of spacecraft, *vertical take-off and landing* (VTOL) *uncrewed aerial vehicles* (UAVs), and microrobotic flyers use quaternion-based control laws [1]–[21]. Controllers based on the use of *attitude-error quaternions* (AEQs) exhibit numerous advantages compared to control methods that use Euler angles and rotation matrices [22], [23]. In particular, quaternions eliminate singularity issues inherent to attitude representations that use Euler angles and provide a compact four-element storage format instead of the nine-element format of rotation matrices. These characteristics improve numerical robustness and decrease computational complexity, enabling faster sampling rates for real-time control [24]–[26]. However, overlapping of the rotational state-space induces a well-known ambiguity problem characterized by the existence of two different symmetric quaternions that can be used to represent the same attitude of an object in space. In particular, we show in [8], [9] that when quaternion-based attitude representations are used in a *closed-loop* (CL) scheme developed to control rigid-body flyers, the resulting dynamical systems have two different equilibria; one asymptotically stable and another unstable, depending on the definiteness—positive or negative—of a controller-gain matrix. Therefore, the stability of these two equilibria can be interchanged in real time by simply multiplying a term in the control law by -1. It is important to note that, even though both possible stable CL equilibrium AEQs represent exactly the same control error, the rotational trajectories required to eliminate this error are different; one has exactly the same direction of the instantaneous Euler axis of the first AEQ whereas the other has the opposite direction of the instantaneous Euler axis of the first AEQ.

In the case discussed in [8], [9], the existence of two fixed points with opposite stability properties and the utilization of real-time switching do not represent a problem because if a trajectory were to start at the unstable equilibrium, any perturbation—large or small—would cause the system state to asymptotically converge to the stable one. A main reason for using stability switching is the simultaneous improvement of flight performance and power utilization. Specifically, this technique is commonly used to avoid unwinding [27], a phenomenon characterized by an abrupt 2π-rad rotation, about the AEQ's Euler axis, of the UAV's body-fixed frame during flight. Avoiding unwinding is important during the execution of tasks that require high-performance flight and synchronization, such as high-speed object tracking, precise positioning, and landing on rotating platforms. Power optimization is crucial in long-lasting operations, such as search and rescue, traffic control, and surveillance.

The simplest automatic stability-switching technique can be implemented by including in the control law, which generates the torque inputted to the system, the sign of the scalar part of the AEQ [8]–[16]. In particular, by multiplying this signum function and a term proportional to the vector part of the AEQ in the definition of the control law in [8], [9], we ensure that this new resulting term generates a torque in the direction of the shorter rotational trajectory required to eliminate the attitude error. However, as discussed in [28], applying a torque in the direction of the shorter rotational trajectory required to eliminate the attitude error does not necessarily ensure the best flight performance because, depending on the current angular velocity and orientation of the UAV, it might be more advantageous to apply a torque in the direction of the longer rotational path. For example, [28] proposes a set of *a-priori* rules for selecting the direction of the instantaneous control torque inputted during flight that decreases the cost of flight according to a heuristic quantification method. These rules were derived from data obtained through the simulation of maneuvers with different

This work was supported in part by the Joint Center for Aerospace Technology Innovation (JCATI) through Award 172, in part by the Washington State University (WSU) Foundation and the Palouse Club through a Cougar Cage Award to N. O. Pérez-Arancibia, and in part by the WSU Voiland College of Engineering and Architecture through a start-up package to N. O. Pérez-Arancibia.

F. M. F. R. Gonçalves, K. I. Matveev, and N. O. Pérez-Arancibia are with the School of Mechanical and Materials Engineering, Washington State University (WSU), Pullman, WA 99164-2920, USA (e-mail: francisco.goncalves@wsu.edu (F. M. F. R. Gonçalves); matveev@wsu.edu (K. I. Matveev); n.perezarancibia@wsu.edu (N. O. Pérez-Arancibia)). R. M. Bena is with the Department of Aerospace and Mechanical Engineering, University of Southern California (USC), Los Angeles, CA 90089-1453, USA (e-mail: bena@usc.edu).

orientation and angular-velocity initial conditions.

Also, the problem can be approached with the methods presented in [29] and [30]. The research presented in [29] developed two methods for synthesizing hybrid controllers aiming to minimize the cost of flight, respectively based on energy-like and backstepping Lyapunov functions, while [30] introduces a switching controller aiming to minimize the cost of flight, explicitly quantified by a function of the angular-velocity and attitude-tracking errors during operation. With the exception of the method in [28], which selects the CL equilibrium AEQ off line using trajectory information known *a priori*, all other CL-fixed-point selection algorithms use instantaneous state information only. Here, we introduce an alternative approach based on *model predictive selection* (MPS), according to which a real-time controller employs a dynamic model of the controlled UAV to estimate the system's state evolution and predict the most cost-efficient stable CL equilibrium AEQ over a finite-time horizon, according to a *performance figure of merit* (PFM). The main contributions of this paper are: (i) a new model-predictive method for the selection of the most cost-efficient, according to a chosen PFM, stable CL equilibrium AEQ over a finite-time horizon; and, to our best knowledge, (ii) the presentation of the first real-time flight-test results that demonstrate the operation and performance of a controller that dynamically selects the stable CL equilibrium AEQ of a UAV during flight.

The rest of the paper is organized as follows. Section II describes the kinematics and dynamics of the UAV used in the presented research, discusses the structure of a continuous controller used as the starting point in the analyses that follow, and presents the stability analysis of the two CL equilibrium AEQs of the system. Section III describes the performance problem associated with the selection of the stable CL equilibrium AEQ and the controller used as benchmark to analyze the experimental results. Section IV introduces the proposed MPS-based controller. Section V presents and discusses experimental results obtained using both the MPS-based and benchmark controllers. Last, Section VI states some conclusions regarding the presented research.

Notation:

1) Italic lowercase symbols represent scalars, e.g., p; bold lowercase symbols represent vectors, e.g., $\boldsymbol{p}$; bold uppercase symbols represent matrices, e.g., $\boldsymbol{P}$; and bold crossed lowercase symbols represent quaternions, e.g., $\boldsymbol{\mathfrak{p}}$.
2) The real variable t denotes continuous time. The integer variables i and k are used to index discrete time.
3) Differentiation with respect to time is denoted by the dot operator, e.g., $\dot{p} = \frac{dp}{dt}$.
4) The symbol $\times$ denotes the cross-product of two vectors. Multiplication between two quaternions is denoted by $\otimes$.
5) The 2-norm of a vector is denoted by the operator $\|\cdot\|_2$.
6) The transpose of a matrix is denoted by $[\,\cdot\,]^T$.
7) The operator sgn $\{\cdot\}$ extracts the sign of a scalar.

II. Dynamic Model and Continuous Controller

A. Reduced-Complexity Rigid-Body Attitude Dynamics

The UAV used in the research presented in this paper is shown in Fig. 1. Also, this figure graphically defines

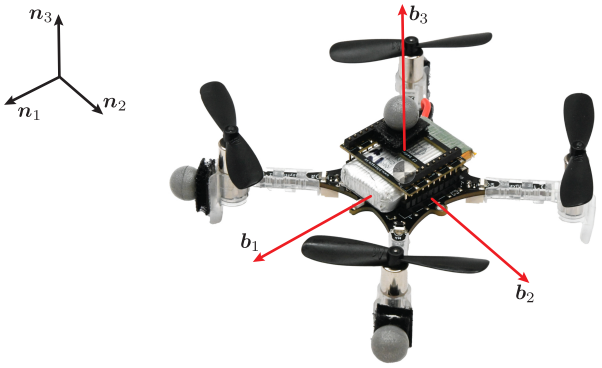

Fig. 1. **Photograph of the UAV platform used in the flight tests, the Crazyflie 2.1, and depiction of the frames of reference used to describe its kinematics.** $\mathcal{N} = \{\boldsymbol{n}_1, \boldsymbol{n}_2, \boldsymbol{n}_3\}$ denotes the inertial frame of reference; $\mathcal{B} = \{\boldsymbol{b}_1, \boldsymbol{b}_2, \boldsymbol{b}_3\}$ denotes the body-fixed frame of reference, whose origin coincides with the center of mass of the UAV.

the inertial and body-fixed frames, $\mathcal{N} = \{\boldsymbol{n}_1, \boldsymbol{n}_2, \boldsymbol{n}_3\}$ and $\mathcal{B} = \{\boldsymbol{b}_1, \boldsymbol{b}_2, \boldsymbol{b}_3\}$, employed to describe the kinematics of the UAV during flight. The origin of $\mathcal{B}$ coincides with the location of the robot's center of mass. Here, we focus only on the attitude dynamics of the flyer, which we represent using the model thoroughly discussed in [1]–[9]. Namely, using quaternion-based attitude representation and D'Alembert's laws, the open-loop state-space dynamics of the system can be written as

$$\begin{aligned} \dot{\boldsymbol{q}} &= \frac{1}{2}\boldsymbol{q} \otimes \begin{bmatrix} 0 \\ \boldsymbol{\omega} \end{bmatrix}, \\ \dot{\boldsymbol{\omega}} &= \boldsymbol{J}^{-1}\left(\boldsymbol{\tau} - \boldsymbol{\omega} \times \boldsymbol{J}\boldsymbol{\omega}\right), \end{aligned} \tag{1}$$

in which $\boldsymbol{q}$ is a unit quaternion that stores the attitude of $\mathcal{B}$ relative to $\mathcal{N}$; $\boldsymbol{\omega}$ is the angular velocity of $\mathcal{B}$ relative to $\mathcal{N}$, written in $\mathcal{B}$; $\boldsymbol{J}$ is the inertia matrix of the robot written in $\mathcal{B}$; and $\boldsymbol{\tau}$ is the aerodynamic-torque input signal computed by the controller. As it is well known [31]–[33],

$$\boldsymbol{q} = \begin{bmatrix} \cos\frac{\Theta}{2} \\ \boldsymbol{u}\sin\frac{\Theta}{2} \end{bmatrix}, \tag{2}$$

where, the unit vector $\boldsymbol{u}$ is the Euler rotation axis and Θ is the rotation amount about $\boldsymbol{u}$ required to represent $\mathcal{B}$ in space relative to $\mathcal{N}$ [31].

B. Structure of Basic Continuous Controller

For the purpose of controller synthesis and implementation, we define the AEQ as

$$\boldsymbol{q}_\mathrm{e} = \boldsymbol{q}^{-1} \otimes \boldsymbol{q}_\mathrm{d}, \tag{3}$$

where $\boldsymbol{q}_\mathrm{e} = \begin{bmatrix} m_\mathrm{e} & \boldsymbol{n}_\mathrm{e}^T \end{bmatrix}^T$ represents the attitude of the *desired* body-fixed frame, $\mathcal{B}_\mathrm{d}$, relative to the *actual* body-fixed frame, $\mathcal{B}$. Consistently, $\boldsymbol{q}$ is the measured instantaneous attitude of $\mathcal{B}$ relative to $\mathcal{N}$, and $\boldsymbol{q}_\mathrm{d}$ represents the instantaneous attitude of $\mathcal{B}_\mathrm{d}$ relative to $\mathcal{N}$. Note that for

$$m_\mathrm{e} = \cos\frac{\Theta_\mathrm{e}}{2} \quad \text{and} \quad \boldsymbol{n}_\mathrm{e} = \boldsymbol{u}_\mathrm{e}\sin\frac{\Theta_\mathrm{e}}{2}, \tag{4}$$

$\boldsymbol{u}_\mathrm{e}$ is the unit vector about which the robot must rotate an amount Θ_e to reach $\mathcal{B}_\mathrm{d}$ from $\mathcal{B}$. During flight, the control

algorithm computes the desired angular velocity of the robot, written in $\mathcal{B}_\mathrm{d}$, as

$$\begin{bmatrix} 0 \\ \hat{\boldsymbol{\omega}}_\mathrm{d} \end{bmatrix} = 2\boldsymbol{q}_\mathrm{d}^{-1} \otimes \dot{\boldsymbol{q}}_\mathrm{d}. \tag{5}$$

Then, to obtain the desired angular velocity of the robot in $\mathcal{B}$, we use the transformations $\boldsymbol{S}_\mathrm{d}$ and $\boldsymbol{S}^T$ as defined in [8]; $\boldsymbol{S}_\mathrm{d}$ transforms vectors from $\mathcal{B}_\mathrm{d}$ to $\mathcal{N}$ and $\boldsymbol{S}^T$ transforms vectors from $\mathcal{N}$ to $\mathcal{B}$. Consequently, $\boldsymbol{\omega}_\mathrm{d} = \boldsymbol{S}^T\boldsymbol{S}_\mathrm{d}\hat{\boldsymbol{\omega}}_\mathrm{d}$. Last, the aerodynamic-torque input is computed according to the continuous control law

$$\boldsymbol{\tau} = \boldsymbol{K_n}\boldsymbol{n}_\mathrm{e} + \boldsymbol{K_\omega}\boldsymbol{\omega}_\mathrm{e} + \boldsymbol{J}\dot{\boldsymbol{\omega}}_\mathrm{d} + \boldsymbol{\omega} \times \boldsymbol{J}\boldsymbol{\omega}, \tag{6}$$

where $\boldsymbol{K_n}$ and $\boldsymbol{K_\omega}$ are positive-definite matrices; $\boldsymbol{\omega}_\mathrm{d}$ is the angular-velocity reference for $\mathcal{B}$; $\boldsymbol{\omega}_\mathrm{e}$ is the angular-velocity tracking error given by $\boldsymbol{\omega}_\mathrm{d} - \boldsymbol{\omega}$; $\boldsymbol{J}\dot{\boldsymbol{\omega}}_\mathrm{d}$ is a feedforward term used for faster tracking performance; and, $\boldsymbol{\omega} \times \boldsymbol{J}\boldsymbol{\omega}$ cancels the nonlinear term in the second line of (1).

C. Closed-Loop Fixed Points and Stability Analysis

By differentiating (3) and substituting the *right-hand side* (RHS) of (6) into the last row of (1), we obtain the closed-loop attitude dynamics of the system. Namely,

$$\begin{aligned} \dot{\boldsymbol{q}}_\mathrm{e} &= \frac{1}{2}\begin{bmatrix} 0 \\ \boldsymbol{\omega}_\mathrm{e} \end{bmatrix} \otimes \boldsymbol{q}_\mathrm{e}, \\ \dot{\boldsymbol{\omega}}_\mathrm{e} &= -\boldsymbol{J}^{-1}\left(\boldsymbol{K_n}\boldsymbol{n}_\mathrm{e} + \boldsymbol{K_\omega}\boldsymbol{\omega}_\mathrm{e}\right). \end{aligned} \tag{7}$$

This state-space system is autonomous and its state is composed of seven variables. Also, as discussed in [8], [9], the vector functions on the RHS of (7) are Lipschitz continuous for appropriately chosen references $\boldsymbol{q}_\mathrm{d}$ and $\boldsymbol{\omega}_\mathrm{d}$. The two fixed points of (7) can be found using the method described in [8]; the first corresponds to $\boldsymbol{q}_\mathrm{e}^\star = [+1\ 0\ 0\ 0]^T$ and $\boldsymbol{\omega}_\mathrm{e}^\star = [0\ 0\ 0]^T$, and the second corresponds to $\boldsymbol{q}_\mathrm{e}^\dagger = [-1\ 0\ 0\ 0]^T$ and $\boldsymbol{\omega}_\mathrm{e}^\star = [0\ 0\ 0]^T$. These two equilibria represent the same attitude and angular-velocity tracking errors; therefore, convergence to either of them represents convergence to the same physical orientation. The stability properties of the first fixed point, $\{\boldsymbol{q}_\mathrm{e}^\star, \boldsymbol{\omega}_\mathrm{e}^\star\}$, can be determined using the method presented in [8], [9], where we invoke *Lyapunov's direct method* and *LaSalles's invariance principle*, as stated by Theorem 4.1 and Corollary 4.1 in [34].

Proposition 1. *Let the attitude and angular-velocity references, $\boldsymbol{q}_\mathrm{d}$ and $\boldsymbol{\omega}_\mathrm{d}$, be smooth functions of time, and let $\boldsymbol{K_n}$ and $\boldsymbol{K_\omega}$ be constant positive-definite matrices. Then, the fixed point $\{\boldsymbol{q}_\mathrm{e}^\star, \boldsymbol{\omega}_\mathrm{e}^\star\}$ of the closed-loop attitude dynamics specified by (7), with $\boldsymbol{q}_\mathrm{e}^\star = [+1\ 0\ 0\ 0]^T$ and $\boldsymbol{\omega}_\mathrm{e}^\star = [0\ 0\ 0]^T$, is asymptotically stable.*

Proof. See Section 3.6 in [8].

As thoroughly discussed in [8], the proof of Proposition 1 relies on two logical steps. First, we show that $\{\boldsymbol{q}_\mathrm{e}^\star, \boldsymbol{\omega}_\mathrm{e}^\star\}$ is locally asymptotically stable; then, we show that $\{\boldsymbol{q}_\mathrm{e}^\dagger, \boldsymbol{\omega}_\mathrm{e}^\star\}$ is unstable and, therefore, any deviation from it always makes the state of the closed-loop attitude dynamics converge to the stable equilibrium point, $\{\boldsymbol{q}_\mathrm{e}^\star, \boldsymbol{\omega}_\mathrm{e}^\star\}$. Also, in [8], we prove the instability of $\{\boldsymbol{q}_\mathrm{e}^\dagger, \boldsymbol{\omega}_\mathrm{e}^\star\}$, using *Lyapunov's indirect method* as stated in Theorem 4.7 of [34]. Here, we formally state this result through a proposition.

Proposition 2. *Let the same conditions of Proposition 1 apply. Then, the fixed point $\{\boldsymbol{q}_\mathrm{e}^\dagger, \boldsymbol{\omega}_\mathrm{e}^\star\}$, with $\boldsymbol{q}_\mathrm{e}^\dagger = [-1\ 0\ 0\ 0]^T$ and $\boldsymbol{\omega}_\mathrm{e}^\star = [0\ 0\ 0]^T$, is unstable.*

Proof. See Appendix C in [8].

III. The Performance Problem and Benchmark Controller

As mentioned in Section II, both CL equilibrium AEQs of the system specified by (7), $\{\boldsymbol{q}_\mathrm{e}^\star, \boldsymbol{\omega}_\mathrm{e}^\star\}$ and $\{\boldsymbol{q}_\mathrm{e}^\dagger, \boldsymbol{\omega}_\mathrm{e}^\star\}$, correspond exactly to the same physical state of the controlled UAV; namely, the condition when the instantaneous position, attitude, and angular velocity of $\mathcal{B}$ coincide exactly with those of $\mathcal{B}_\mathrm{d}$. However, the first fixed point is stable whereas the second is unstable. This apparent paradox results from the quaternion-ambiguity phenomenon. To see this issue, consider (4) and recall that $\boldsymbol{u}_\mathrm{e}$ is the unit vector about which $\mathcal{B}$ must be rotated an angle Θ_e to exactly reach the attitude of $\mathcal{B}_\mathrm{d}$. Therefore, Propositions 1 and 2 tell us that when $\Theta_\mathrm{e} = 0$ and $\boldsymbol{\omega}_\mathrm{e} = \boldsymbol{0}$, small deviations from this condition are easily corrected by the system's controller; whereas, when $\Theta_\mathrm{e} = 2\pi$ rad and $\boldsymbol{\omega}_\mathrm{e} = \boldsymbol{0}$, any deviation from this condition, small or large, induces the system's controller to generate a rotation on the order of 2π rad. Furthermore, it is straightforward to see that when $\pi < \Theta_\mathrm{e} < 2\pi$ rad, the torque $\boldsymbol{K_n}\boldsymbol{n}_\mathrm{e}$ is applied in the direction of the longer path. This dynamic behavior does not pose any problems regarding stability; however, from a performance perspective, it raises numerous energy and state-error optimization research questions.

In the past, to avoid undesired 2π-rad rotations during the execution of flight maneuvers [27], we modified the first term of the control law specified by (6) by multiplying it by the sign of m_e [7]–[11]. Namely,

$$\boldsymbol{\tau}_\mathrm{b} = \mathrm{sgn}\{m_\mathrm{e}\}\boldsymbol{K_n}\boldsymbol{n}_\mathrm{e} + \boldsymbol{K_\omega}\boldsymbol{\omega}_\mathrm{e} + \boldsymbol{J}\dot{\boldsymbol{\omega}}_\mathrm{d} + \boldsymbol{\omega} \times \boldsymbol{J}\boldsymbol{\omega}. \tag{8}$$

From this point onwards, we refer to (8) as the benchmark controller. Clearly, the direction of the torque $\mathrm{sgn}\{m_\mathrm{e}\}\boldsymbol{K_n}\boldsymbol{n}_\mathrm{e}$ is the same as that of $\boldsymbol{u}_\mathrm{e}$, for $0 \leq \Theta_\mathrm{e} < \pi$, and is that of $-\boldsymbol{u}_\mathrm{e}$, for $\pi \leq \Theta_\mathrm{e} < 2\pi$, which ensures that the torque $\mathrm{sgn}\{m_\mathrm{e}\}\boldsymbol{K_n}\boldsymbol{n}_\mathrm{e}$ is applied in the direction of the shorter rotational path between $\mathcal{B}$ and $\mathcal{B}_\mathrm{d}$. An alternative interpretation of the switching method specified by (8) is that when $\mathrm{sgn}\{m_\mathrm{e}\}$ becomes negative, $\{\boldsymbol{q}_\mathrm{e}^\dagger, \boldsymbol{\omega}_\mathrm{e}^\star\}$ becomes asymptotically stable and $\{\boldsymbol{q}_\mathrm{e}^\star, \boldsymbol{\omega}_\mathrm{e}^\star\}$ unstable. This stability property of the system is reversed when $\mathrm{sgn}\{m_\mathrm{e}\}$ switches back to positive. There is ample evidence that this method is highly effective and robust in real-time flight applications [7]–[11]. However, it does not guarantee the best performance regarding the control effort, which is directly related to energy consumption. We hypothesize that replacing $\mathrm{sgn}\{m_\mathrm{e}\}$ with a function that predicts the most cost-efficient direction of the first term in the torque control input might be a better option. This is the motivation for introducing the MPS-based controller discussed next.

IV. Model Predictive Selection

To our best knowledge, all the published methods that select the stable CL equilibrium AEQ during flight use the current value of the system state only [29], [30]. Here, we introduce the MPS algorithm, an alternative approach that predicts and selects the most cost-efficient stable CL

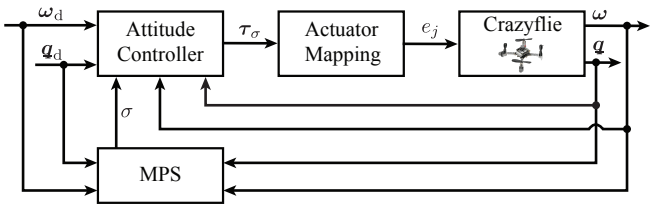

Fig. 2. **Block Diagram of the MPS-based Control Scheme.** The MPS algorithm receives as inputs the attitude-reference quaternion, measured quaternion, angular-velocity reference, and measured angular velocity; then, it selects the value of σ and sends it to the attitude controller, which computes the aerodynamic-torque control input, $\boldsymbol{\tau}_\sigma$. Last, the actuator mapping receives as input $\boldsymbol{\tau}_\sigma$ and maps it into the *pulse width modulation* (PWM) signals, e_j, for $j \in \{1, 2, 3, 4\}$, that excite the DC motors of the flyer as described in [1].

equilibrium AEQ over a finite-time horizon, according to a PFM. In this case, we use the PFM

$$\Gamma(t) = \int_t^{t+t_{\rm h}} \left[\boldsymbol{\tau}_\sigma^T(\zeta) \boldsymbol{R} \boldsymbol{\tau}_\sigma(\zeta) + \boldsymbol{n}_{\rm e}^T(\zeta) \boldsymbol{Q} \boldsymbol{n}_{\rm e}(\zeta) \right] d\zeta, \quad (9)$$

where $t_{\rm h}$ is the time horizon; $\boldsymbol{\tau}_\sigma$ is the torque exciting the system, which is generated through a control law that explicitly depends on the parameter σ; and, $\boldsymbol{R}$ and $\boldsymbol{Q}$ are Hermitian positive-definite weight matrices that function as tuning parameters. We specify the control law as

$$\boldsymbol{\tau}_\sigma = \sigma \boldsymbol{K}_{\boldsymbol{n}} \boldsymbol{n}_{\rm e} + \boldsymbol{K}_{\boldsymbol{\omega}} \boldsymbol{\omega}_{\rm e} + \boldsymbol{J} \dot{\boldsymbol{\omega}}_{\rm d} + \boldsymbol{\omega} \times \boldsymbol{J} \boldsymbol{\omega}, \quad (10)$$

where $\sigma \in \{-1, +1\}$ is dynamically selected according to

$$\sigma^+ = \begin{cases} \sigma, & \text{if} \quad -\delta < \Delta\Gamma < \delta \\ -1, & \text{if} \quad \Delta\Gamma \geq \delta \\ +1, & \text{if} \quad \Delta\Gamma \leq -\delta \end{cases}, \quad (11)$$

where σ is the current value, initialized as $\sigma = +1$; $\delta > 0$ is a hysteresis margin included to avoid Zeno behavior [35]; and, $\Delta\Gamma = \Gamma^\star - \Gamma^\dagger$, in which $\Gamma^\star$ and $\Gamma^\dagger$ are the PFM values, computed using (9), associated with choosing either $\{\boldsymbol{q}_{\rm e}^\star, \boldsymbol{\omega}_{\rm e}^\star\}$ or $\{\boldsymbol{q}_{\rm e}^\dagger, \boldsymbol{\omega}_{\rm e}^\star\}$ as the stable CL equilibrium AEQ, respectively.

Since the possible trajectories of $\boldsymbol{\tau}_\sigma(t)$ and $\boldsymbol{n}_{\rm e}(t)$, for $t \in [t : t + t_{\rm h}]$, are unknown at time t, in order to compute $\Gamma^\star$ and $\Gamma^\dagger$, we estimate them using the model specified by (1)–(7). Specifically, using (1)–(7) and (10), we simulate the trajectory of the UAV during the time range specified by a finite-time horizon, $t_{\rm h}$, for both $\sigma = +1$ and $\sigma = -1$, and then select the stable CL equilibrium AEQ associated with the lesser cost of performing the corresponding maneuver, according to the PFM specified by (9). The prediction algorithm is based on the methods in Chapter 12 of [36] and we briefly describe them here. First, since the algorithm is implemented on a *digital signal processor* (DSP), we define $\boldsymbol{x}(i) = \left[\boldsymbol{q}_{\rm e}^T(i) \ \boldsymbol{\omega}_{\rm e}^T(i)\right]^T$, where $\boldsymbol{q}_{\rm e}(i)$ and $\boldsymbol{\omega}_{\rm e}(i)$ are the sampled versions of $\boldsymbol{q}_{\rm e}(t)$ and $\boldsymbol{\omega}_{\rm e}(t)$, respectively. Then, we define $\boldsymbol{x}_{i+k|i}$ as the state at discrete time $i + k$ predicted at discrete time i, with the starting point $\boldsymbol{x}_{i|i} = \boldsymbol{x}(i)$. Next, we solve $\boldsymbol{x}_{i+k+1|i} = \boldsymbol{f}(\boldsymbol{x}_{i+k|i})$, with $k \in [0 : i_{\rm h} - 1]$, for the sequences $\boldsymbol{q}_{\rm e}(i)$ and $\boldsymbol{\omega}_{\rm e}(i)$, with $i \in [i : i + i_{\rm h}]$, where $i_{\rm h}$ is the discrete-time horizon corresponding to the continuous $t_{\rm h}$ and $\boldsymbol{f}(\boldsymbol{x})$ denotes the sampled version of the RHS vector function in (7). At each time instant, we predict the evolution of the system state for the two possible inputs, $\boldsymbol{\tau}_{+1}$ and $\boldsymbol{\tau}_{-1}$, associated with choosing either $\{\boldsymbol{q}_{\rm e}^\star, \boldsymbol{\omega}_{\rm e}^\star\}$ or $\{\boldsymbol{q}_{\rm e}^\dagger, \boldsymbol{\omega}_{\rm e}^\star\}$ as the stable CL equilibrium AEQ. Last, we use these predictions to execute the selection rule specified by (11).

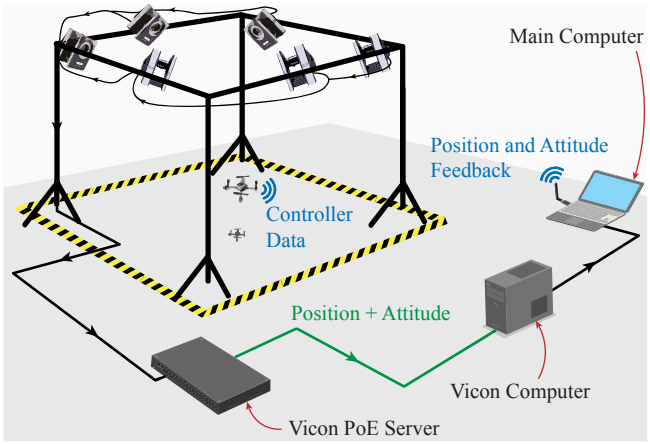

Fig. 3. **Experimental setup used in the flight tests.** Illustration of the flying arena and signals-and-systems diagram. The setup is equipped with a six-V5-camera Vicon motion-capture system, which is used to measure the position and attitude of the UAV during flight at a rate of 500 Hz. These data are then sent, via the Vicon PoE server, to the Vicon computer, which records and transmits the data to the main computer using the *virtual-reality peripheral network* (VRPN) interface. Last, the main computer transmits the position and attitude real-time data to the UAV, using the Python-Crazyflie-Client library, via radio at approximately 50 Hz. The UAV transmits the signals generated by the online controller to the main computer using radio communication.

The MPS-based control scheme is shown in Fig. 2. We do not provide a rigorous and detailed stability proof of this scheme here; however, we state some basic facts regarding this matter. The inclusion of the hysteresis margin, δ, in the definition of the switching law specified by (11) prevents the system from becoming unstable due to chattering. Once chattering is avoided, as long as the responses of the two closed-loop subsystems corresponding to $\sigma = -1$ and $\sigma = +1$ approach zero as time increases, the switching closed-loop system corresponding to the control law specified by (10), as a whole, remains stable. This conclusion follows from noticing that each switching event can be thought of as the reinitialization of one of the two subsystems with a finite initial condition. The experimental results presented in Section V provide strong evidence supporting this statement.

V. Real-Time Flight Experiments

A. Experimental Setup

The flying arena used in the flight tests discussed in Section V-B is depicted in Fig. 3. This setup is instrumented with a six-V5-camera Vicon motion-capture system running at 500 Hz. These cameras measure the position and attitude of the UAV during flight. Then, these data are fused with the angular-velocity signal, which is measured with an onboard BMIO88 *inertial measurement unit* (IMU) sensor, using the extended Kálmán filter in [37], [38]. Specifically, the position and attitude of the UAV are sent to a processing server (Vicon PoE) and, then, to the Vicon computer that runs Tracker 3.9 (software). The Vicon computer communicates with the main computer of the setup through the *virtual-reality peripheral network* (VRPN) protocol. Last, the main computer transmits the Vicon measured data to the

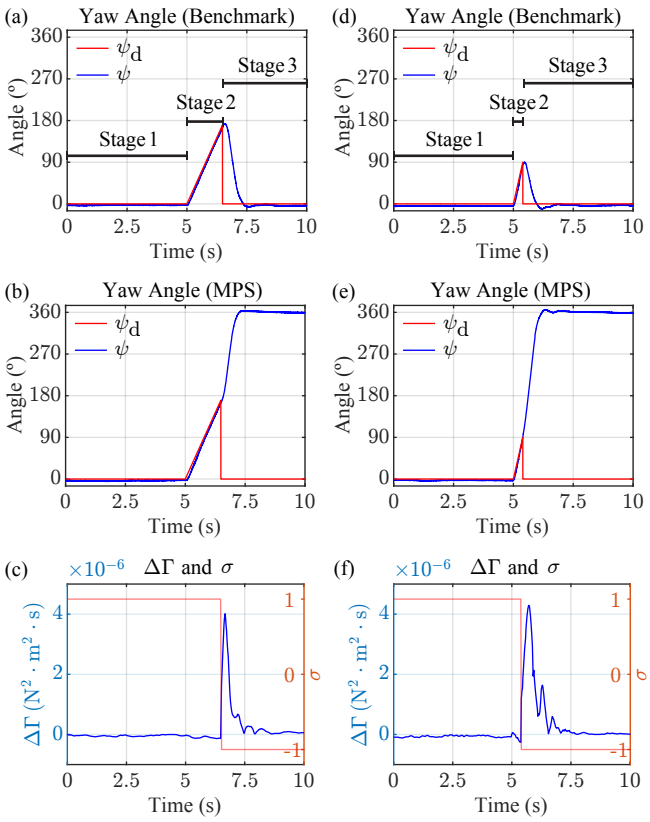

Fig. 4. **Experimental signals corresponding to two different attitude references and two different controllers. (a)** Real-time yaw reference and measured yaw signal for the parameter pair $\{2 \cdot \boldsymbol{b}_3 \text{ rad} \cdot \text{s}^{-1}, 170°\}$ and benchmark controller. **(b)** Real-time yaw reference and measured yaw signal for the parameter pair $\{2 \cdot \boldsymbol{b}_3 \text{ rad} \cdot \text{s}^{-1}, 170°\}$ and MPS-based controller. **(c)** Real-time $\Delta\Gamma$ and σ signals corresponding to the case in (b), i.e., $\{2 \cdot \boldsymbol{b}_3 \text{ rad} \cdot \text{s}^{-1}, 170°\}$. **(d)** Real-time yaw reference and measured yaw signal for the parameter pair $\{4 \cdot \boldsymbol{b}_3 \text{ rad} \cdot \text{s}^{-1}, 90°\}$ and benchmark controller. **(e)** Real-time yaw reference and measured yaw signal for the parameter pair $\{4 \cdot \boldsymbol{b}_3 \text{ rad} \cdot \text{s}^{-1}, 90°\}$ and MPS-based controller. **(f)** Real-time $\Delta\Gamma$ and σ signals corresponding to the case in (e), i.e., $\{4 \cdot \boldsymbol{b}_3 \text{ rad} \cdot \text{s}^{-1}, 90°\}$.

UAV via radio, using a Bitcraze antenna (Crazyradio PA) and the Python-Crazyflie-Client library at approximately 50 Hz. The UAV transmits the signals generated by the online controller to the main computer using radio communication. Both the proposed MPS-based and benchmark controllers are run onboard at a rate of 500 Hz. During flight, the position of the UAV is controlled using the scheme described in [8], [9].

B. Flight Experiments

To test and demonstrate the capabilities of the proposed MPS-based controller, we performed several different high-speed yaw-tracking maneuvers. The results corresponding to two different real-time attitude references are shown in Fig. 4. Each reference is composed of three stages. In Stage 1, the quadrotor hovers stationarily and the rotational commands are set to zero; in Stage 2, an angular-velocity reference in the $\boldsymbol{b}_3$ direction commands the UAV to rotate at the constant value $\boldsymbol{\omega}_0$ about its yaw axis; last, in Stage 3, once the yaw-angle signal $\psi(t)$, with the form of a ramp, reaches a desired *initial* angle $\psi(t_0) = \psi_0$, the constant yaw-angle reference $\psi_\text{d}(t) = 0°$, for $t \geq t_0$, is inputted to the system, thus compelling the UAV to rotate toward it. Executing pure yaw-tracking maneuvers allows us to straightforwardly evaluate the functionality and performance of different control methods. For the real-time implementation of the controllers, we selected $\boldsymbol{K_n} = 900 \cdot \boldsymbol{J}$ N · m and $\boldsymbol{K_\omega} = 90 \cdot \boldsymbol{J}$ N · m · s · rad^{-1} as the controller gains in (8) and (10). Additionally, we empirically selected the finite-time horizon for the MPS-based controller to be 0.4 s, and the tunable weights in (9) to be $\boldsymbol{R} = \boldsymbol{I}$ and $\boldsymbol{Q} = 10^{-6} \cdot \boldsymbol{I}$ N^2 · m^2, where $\boldsymbol{I}$ is the identity matrix with compatible dimensions. The reason for choosing significantly lower values for the diagonal entries of $\boldsymbol{Q}$ is the difference in order of magnitude between $\boldsymbol{\tau}_\sigma^T \boldsymbol{\tau}_\sigma$ and $\boldsymbol{n}_\text{e}^T \boldsymbol{n}_\text{e}$. Last, we set the hysteresis margin to be $\delta = 5 \cdot 10^{-7}$, which was empirically determined to be large enough to avoid chattering.

The data in Figs. 4(a)-(c) correspond to an attitude reference defined by the pair $\{\boldsymbol{\omega}_0 = 2 \cdot \boldsymbol{b}_3 \text{ rad} \cdot \text{s}^{-1}, \psi_0 = 170°\}$. Fig. 4(a) shows the reference ψ_d and measurement ψ, when the UAV is flown by the benchmark controller. Fig. 4(b) shows the reference ψ_d and measurement ψ, when the UAV is flown by the MPS-based controller. For this value of ψ_0, the MPS-based controller forces the UAV to continue rotating in the direction of $\boldsymbol{u}_\text{e}$ and not reverse its rotation when the attitude reference drastically changes, whereas the benchmark controller forces the UAV to reverse its direction of rotation when the attitude reference drastically changes. Fig. 4(c) shows the time evolution of signals $\Delta\Gamma$ and σ corresponding to the data in Fig. 4(b), obtained with the MPS-based controller. Since the controllers are implemented on a DSP, to evaluate and compare the flight performances achieved with the MPS-based and benchmark controllers, we use a discrete-time version of the PFM specified by (9), over the time interval during which the maneuver is executed. Namely,

$$\Gamma_\text{exp} = \sum_{i=1}^{N_\text{s}} \left[\boldsymbol{\tau}_\text{exp}^T(i) \boldsymbol{R} \boldsymbol{\tau}_\text{exp}(i) + \boldsymbol{n}_\text{e,exp}^T(i) \boldsymbol{Q} \boldsymbol{n}_\text{e,exp}(i) \right] \cdot T_\text{s}, \quad (12)$$

where N_s is the number of samples collected during the flight maneuver and T_s is the sampling time. In all cases discussed here, $N_\text{s} = 1500$ and $T_\text{s} = 0.002$ s. The subscript 'exp' simply means 'experimental.' For the cases in Figs. 4(a)-(c), the experimental PFM for the benchmark controller is 2.78×10^{-5} N^2 · m^2 · s, and for the MPS-based controller is 6.25×10^{-6} N^2 · m^2 · s. Video footage of the two flight tests corresponding to Figs. 4(a) and (b) are shown in the accompanying supplementary movie. Also, Fig. 5 shows photographic sequences of these two experiments. Here, the superior performance of the MPS-based controller over the benchmark scheme is evident.

The data in Figs. 4(d)-(f) correspond to an attitude reference defined by the pair $\{\boldsymbol{\omega}_0 = 4 \cdot \boldsymbol{b}_3 \text{ rad} \cdot \text{s}^{-1}, \psi_0 = 90°\}$. Fig. 4(d) shows the reference ψ_d and measurement ψ, when the UAV is flown by the benchmark controller. Fig. 4(e) shows the reference ψ_d and measurement ψ, when the UAV is flown by the MPS-based controller. For this value of ψ_0, the MPS-based controller forces the UAV to continue rotating in the direction of $\boldsymbol{u}_\text{e}$ and not reverse its rotation when the attitude reference drastically changes, whereas the benchmark controller forces the UAV to reverse its rotation when the attitude reference drastically changes. Fig. 4(f) shows the time evolution of signals $\Delta\Gamma$ and σ corresponding to the data in Fig. 4(e), obtained with the MPS-based controller.

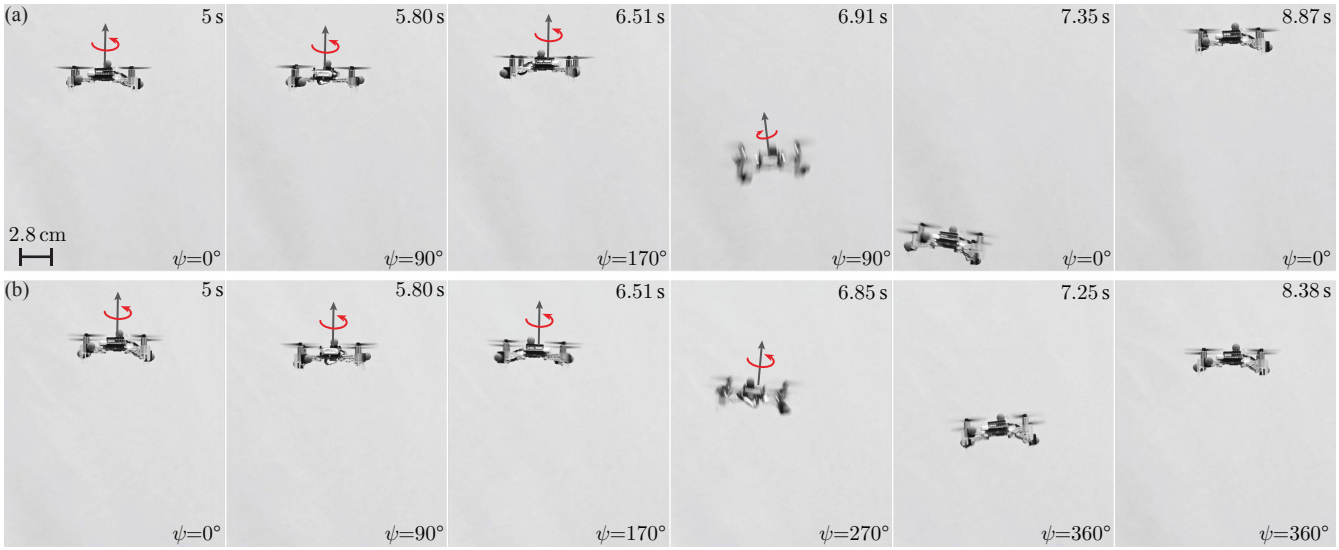

Fig. 5. **Two flight tests performed using the MPS-based controller and benchmark scheme. (a)** Photographic sequence from video footage of a flight test performed using the benchmark controller and the attitude reference defined by the parameter pair $\{2 \cdot \boldsymbol{b}_3 \text{ rad} \cdot \text{s}^{-1}, 170°\}$. The third frame corresponds to the instant when the yaw reference is set to 0°; in this case, the benchmark controller selects $\sigma = +1$, which produces a reverse rotation and performance degradation. **(b)** Photographic sequence from video footage of a flight test performed using the proposed MPS-based controller and the attitude reference defined by the parameter pair $\{2 \cdot \boldsymbol{b}_3 \text{ rad} \cdot \text{s}^{-1}, 170°\}$. The third frame corresponds to the instant when the yaw reference is set to 0°; in this case, the MPS-based method selects $\sigma = -1$, which maintains the current direction of rotation and, thus, leads to high flight performance. These two experiments can be viewed in the accompanying supplementary movie.

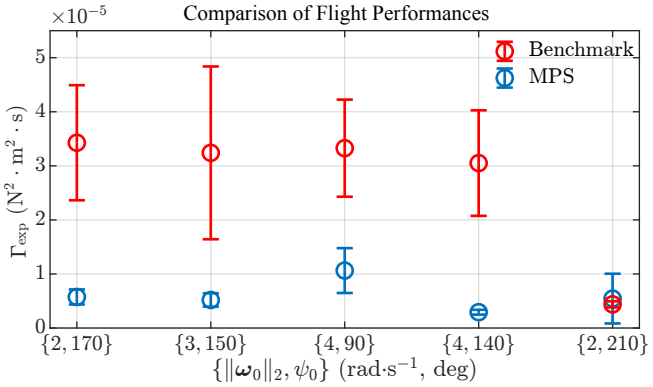

Fig. 6. **Comparison of flight performances obtained using the benchmark and MPS-based controllers.** Each data point represents the mean and *empirical standard deviation* (ESD) of ten Γ_{exp} values corresponding to ten back-to-back flight experiments performed with the same attitude reference and controller.

For the cases in Figs. 4(d)-(f), the experimental PFM for the benchmark controller is $4.82 \times 10^{-5}\,\text{N}^2 \cdot \text{m}^2 \cdot \text{s}$, and for the MPS-based controller is $1.29 \times 10^{-5}\,\text{N}^2 \cdot \text{m}^2 \cdot \text{s}$.

Last, Fig. 6 summarizes ten sets of experimental results obtained during Stage 3 of flight tests. Each experimental result in a set corresponds to a pair of attitude-reference parameters, $\{\boldsymbol{\omega}_0, \psi_0\}$, and a type of controller. Each data point in the plot of Fig. 6 represents the mean and *empirical standard deviation* (ESD) of ten Γ_{exp} values corresponding to ten back-to-back flight experiments performed with the same reference and control system. The data collected using the benchmark controller are shown in red and those collected using the MPS-based controller are shown in blue. These data show that, on average, the MPS-based controller reduces the value of Γ_{exp} by $60.30\,\%$ when compared to the benchmark controller. Furthermore, in all the cases in which the MPS-based and benchmark controllers select different CL equilibrium AEQs, the worst performance obtained with the MPS-based controller is better than the best performance achieved with the benchmark controller. This comparison compellingly demonstrates the superior performance of the proposed MPS-based controller. In the last case, corresponding to the pair $\{\boldsymbol{\omega}_0 = 2 \cdot \boldsymbol{b}_3 \text{ rad} \cdot \text{s}^{-1}, \psi_0 = 210°\}$, the performances achieved by both controllers are very similar because they select the same stable CL equilibrium AEQ. It is worth noting that the ESD values for all benchmark-controller data points are significantly larger than those of the MPS-based-controller data points. This observation is explained by the reverse rotations forced by the former method that the latter method avoids; reverse rotations degrade the flight performance and make repeatability almost impossible.

VI. Conclusions

We presented a new attitude control method that dynamically selects the stable CL equilibrium AEQ of a UAV during high-speed yaw-rotational flight. The main objective of this approach is minimizing the cost of flight according to a PFM that explicitly accounts for both the control input and attitude-error state of the UAV. The method is based on MPS, a new algorithm implemented in real time to estimate the cost of flight over a finite-time horizon, using a dynamic model derived from first principles. To test and demonstrate the functionality and performance of the proposed method, we performed one hundred yaw-tracking flight tests using an MPS-based controller and a benchmark scheme. For these tests, the experimental data show that the MPS-based controller reduces the value of the cost-of-flight PFM by $60.30\,\%$, on average, with respect to that obtained with the benchmark controller. These results highlight the suitability and potentials of the MPS-based approach.

REFERENCES

[1] Y. Chen and N. O. Pérez-Arancibia, "Generation and Real-Time Implementation of High-Speed Controlled Maneuvers Using an Autonomous 19-Gram Quadrotor," in *Proc. IEEE Int. Conf. Robot. Automat. (ICRA)*, Stockholm, Sweden, May 2016, pp. 3204–3211.

[2] ——, "Lyapunov-Based Controller Synthesis and Stability Analysis for the Execution of High-Speed Multi-Flip Quadrotor Maneuvers," in *Proc. Amer. Control Conf. (ACC)*, Seattle, WA, USA, May 2017, pp. 3599–3606.

[3] ——, "Nonlinear Adaptive Control of Quadrotor Multi-Flipping Maneuvers in the Presence of Time-Varying Torque Latency," in *Proc. IEEE/RSJ Int. Conf. Intell. Robot. Syst. (IROS)*, Madrid, Spain, Oct. 2018, pp. 7845–7852.

[4] ——, "Adaptive Control of Aerobatic Quadrotor Maneuvers in the Presence of Propeller-Aerodynamic-Coefficient and Torque-Latency Time-Variations," in *Proc. IEEE Int. Conf. Robot. Automat. (ICRA)*, Montreal, QC, Canada, May 2019, pp. 6447–6453.

[5] ——, "Controller Synthesis and Performance Optimization for Aerobatic Quadrotor Flight," *IEEE Trans. Control Syst. Technol.*, vol. 28, no. 6, pp. 2204–2219, Nov. 2020.

[6] ——, "Adaptive control of a VTOL uncrewed aerial vehicle for high-performance aerobatic flight," *Automatica*, vol. 159, Jan. 2024, Art. no. 109922.

[7] A. A. Calderón, Y. Chen, X. Yang, L. Chang, X.-T. Nguyen, E. K. Singer, and N. O. Pérez-Arancibia, "Control of Flying Robotic Insects: A Perspective and Unifying Approach," in *Proc. 19th Int. Conf. Adv. Robot. (ICAR)*, Belo Horizonte, Brazil, Dec. 2019, pp. 747–754.

[8] R. M. Bena, X. -T. Nguyen, X. Yang, A. A. Calderón, Y. Chen, and N. O. Pérez-Arancibia, "A Multiplatform Position Control Scheme for Flying Robotic Insects," *J. Intell. Robot. Syst.*, vol. 105, no. 1, May 2022, Art. no. 19.

[9] R. M. Bena, X. Yang, A. A. Calderón, and N. O. Pérez-Arancibia, "High-Performance Six-DOF Flight Control of the Bee^{++}: An Inclined-Stroke-Plane Approach," *IEEE Trans. Robot.*, vol. 39, no. 2, pp. 1668–1684, Apr. 2023.

[10] X. Yang, Y. Chen, L. Chang, A. A. Calderón, and N. O. Pérez-Arancibia, "Bee^{+}: A 95-mg Four-Winged Insect-Scale Flying Robot Driven by Twinned Unimorph Actuators," *IEEE Robot. Autom. Lett.*, vol. 4, no. 4, pp. 4270–4277, Oct. 2019.

[11] R. M. Bena, C. Zhao, and Q. Nguyen, "Safety-Aware Perception for Autonomous Collision Avoidance in Dynamic Environments," *IEEE Robot. Autom. Lett.*, vol. 8, no. 12, pp. 7962–7969, Dec. 2023.

[12] S. Salcudean, "A Globally Convergent Angular Velocity Observer for Rigid Body Motion," *IEEE Trans. Autom. Control*, vol. 36, no. 12, pp. 1493–1497, Dec. 1991.

[13] B. Wie and P. M. Barba, "Quaternion Feedback for Spacecraft Large Angle Maneuvers," *J. Guid. Control Dyn.*, vol. 8, no. 3, pp. 360–365, May 1985.

[14] J. Thienel and R. M. Sanner, "A Coupled Nonlinear Spacecraft Attitude Controller and Observer With an Unknown Constant Gyro Bias and Gyro Noise," *IEEE Trans. Autom. Control*, vol. 48, no. 11, pp. 2011–2015, Nov. 2003.

[15] R. Kristiansen, P. J. Nicklasson, and J. T. Gravdahl, "Satellite Attitude Control by Quaternion-Based Backstepping," *IEEE Trans. Control Syst. Technol.*, vol. 17, no. 1, pp. 227–232, Jan. 2009.

[16] O. -E. Fjellstad and T. I. Fossen, "Quaternion Feedback Regulation of Underwater Vehicles," in *Proc. IEEE Int. Conf. Control Appl.*, Glasgow, UK, Aug. 1994, pp. 857–862.

[17] A. Tayebi, "Unit Quaternion-Based Output Feedback for the Attitude Tracking Problem," *IEEE Trans. Autom. Control*, vol. 53, no. 6, pp. 1516–1520, Jul. 2008.

[18] J. Cariño, H. Abaunza, and P. Castillo, "Quadrotor Quaternion Control," in *Proc. Int. Conf. Unmanned Aircr. Syst. (ICUAS)*, Denver, CO, USA, Jun. 2015, pp. 825–831.

[19] Y. Yang, "Spacecraft attitude determination and control: Quaternion based method," *Annu. Rev. Control*, vol. 36, no. 2, pp. 198–219, Dec. 2012.

[20] E. Fresk and G. Nikolakopoulos, "Full Quaternion Based Attitude Control for a Quadrotor," in *2013 Eur. Control Conf. (ECC)*, Zürich, Switzerland, Jul. 2013, pp. 3864–3869.

[21] B. Wie, H. Weiss, and A. Arapostathis, "Quaternion Feedback Regulator for Spacecraft Eigenaxis Rotations," *J. Guid. Control Dyn.*, vol. 12, no. 3, pp. 375–380, May 1989.

[22] N. O. Pérez-Arancibia, P.-E. J. Duhamel, K. Y. Ma, and R. J. Wood, "Model-Free Control of a Flapping-Wing Flying Microrobot," in *Proc. 16th Int. Conf. Adv. Robot. (ICAR)*, Montevideo, Uruguay, Nov. 2013.

[23] ——, "Model-Free Control of a Hovering Flapping-Wing Microrobot," *J. Intell. Robot. Syst.*, vol. 77, no. 1, pp. 95–111, Jan. 2015.

[24] A. Alaimo, V. Artale, C. Milazzo, and A. Ricciardello, "Comparison between Euler and Quaternion Parametrization in UAV Dynamics," in *Proc. AIP Conf.*, vol. 1558, Rhodes, Greece, Oct. 2013, pp. 1228–1231.

[25] J. T.-Y. Wen and K. Kreutz-Delgado, "The Attitude Control Problem," *IEEE Trans. Autom. Control*, vol. 36, no. 10, pp. 1148–1162, Oct. 1991.

[26] R. Dargham, A. Sayouti, and H. Medromi, "Euler and Quaternion Parameterization in VTOL UAV Dynamics with Test Model Efficiency," *Int. J. Appl. Inf. Syst.*, vol. 9, no. 8, pp. 25–28, Oct. 2015.

[27] S. P. Bhat and D. S. Bernstein, "A topological obstruction to continuous global stabilization of rotational motion and the unwinding phenomenon," *Syst. Control Lett.*, vol. 39, no. 1, pp. 63–70, Jan. 2000.

[28] R. Schlanbusch, R. Kristiansen, and P. J. Nicklasson, "On Choosing Quaternion Equilibrium Point in Attitude Stabilization," in *Proc. IEEE Aerosp. Conf.*, Big Sky, MT, USA, Mar. 2010, pp. 1–6.

[29] C. G. Mayhew, R. G. Sanfelice, and A. R. Teel, "Robust Global Asymptotic Attitude Stabilization of a Rigid Body by Quaternion-Based Hybrid Feedback," in *Proc. IEEE Conf. Decis. Control (CDC), Chin. Control Conf. (CCC)*, Shanghai, China, Dec. 2009, pp. 2522–2527.

[30] R. Schlanbusch, A. Loria, and P. J. Nicklasson, "On the stability and stabilization of quaternion equilibria of rigid bodies," *Automatica*, vol. 48, no. 12, pp. 3135–3141, Dec. 2012.

[31] J. B. Kuipers, *Quaternions and Rotation Sequences: A Primer with Applications to Orbits, Aerospace and Virtual Reality*. Princeton, NJ, USA: Princeton University Press, 2002.

[32] F. L. Markley and J. L. Crassidis, *Fundamentals of Spacecraft Attitude Determination and Control*. New York, NY, USA: Springer, 2014.

[33] S. L. Altmann, *Rotations, Quaternions, and Double Groups*. Mineola, NY, USA: Dover Publications, Inc, 1986.

[34] H. K. Khalil, *Nonlinear Systems*. Upper Saddle River, NJ, USA: Prentice-Hall, 2002.

[35] D. Liberzon, *Switching in Systems and Control*. New York, NY, USA: Springer, 2003.

[36] F. Borrelli, A. Bemporad, and M. Morari, *Predictive Control for Linear and Hybrid Systems*. Cambridge, UK: Cambridge Univ. Press, 2017.

[37] M. W. Mueller, M. Hamer, and R. D'Andrea, "Fusing Ultra-Wideband Range Measurements with Accelerometers and Rate Gyroscopes for Quadrocopter State Estimation," in *Proc. IEEE Int. Conf. Robot. Automat. (ICRA)*, Seattle, WA, USA, May 2015, pp. 1730–1736.

[38] M. W. Mueller, M. Hehn, and R. D'Andrea, "Covariance Correction Step for Kalman Filtering with an Attitude," *J. Guid. Control Dyn.*, vol. 40, no. 9, pp. 2301–2306, Sep. 2017.